JMEPEG (2022) 31:542–551
https://doi.org/10.1007/s11665-021-06197-y


1059-9495/$19.00

# A Comparative Study of Microstructures and Mechanical Behavior of Laser Metal Deposited and Electron Beam Melted Ti-6Al-4V

*Mehmood Rashid, R. Lakshmi Narayan, Dan-Li Zhang, and Wei-Zhong Han*

Submitted: 5 April 2021 / Revised: 14 July 2021 / Accepted: 1 August 2021 / Published online: 3 September 2021

**The microstructures and mechanical properties of Ti-6Al-4V fabricated using laser metal deposition (LMD) and electron beam melting (EBM) were investigated and compared. The hardness, strength and work hardening exponent (*n*) of the LMD samples are superior to that of EBM samples. The EBM samples are more ductile, exhibit resistance to rapid plastic strain localization and have uniform hardness throughout the build. A detailed microstructural characterization was conducted for both alloys before and after the tensile tests. The differences in mechanical behavior of the two samples originate from their distinct dislocation densities within α and the relative proportions of Widmanstätten and colony type arrangements of the α+β laths, which in turn are an outcome of the distinct cooling profiles in the two additive manufacturing methods. On the basis of these results, strategies to improve the mechanical properties of both alloys are discussed.**

**Keywords** additive manufacturing, electron beam melting, laser metal deposition, microstructures, Ti-6Al-4V

## 1. Introduction

Powder bed fusion process or powder-based additive manufacturing (AM) of Ti-6Al-4V, where the powdered form of the alloy is joined layer by layer to obtain the desired shape of a component, has several advantages over conventional manufacturing (Ref 1-5). Besides reducing material wastage, overall time of production and saving costs associated with post-processing machining, powder AM methods circumvent the formability issues of Ti-6Al-4V. Powder-based AM is further subdivided into powder bed and powder directed energy deposition (DED) processes. Powder bed processes, such as selective laser melting (SLM) and electron beam melting (EBM), involve melting of powders that are laid over a vertically retracting bed by a laser beam and electron beam, respectively. In powder DED processes, such as laser metal deposition (LMD), the metal powder is injected via a nozzle and simultaneously melted by a laser beam at a target location or substrate. With this mechanism of fabrication, powder DED processes can also be improvised as tools to re-manufacture or restore broken components (Ref 1-5).

**Mehmood Rashid, Dan-Li Zhang,** and **Wei-Zhong Han**, State Key Laboratory for Mechanical Behaviour of Materials, Centre for Advancing Material Performance from the Nanoscale (CAMP-Nano), Xi'an Jiaotong University, 710049 Xian, China; and **R. Lakshmi Narayan**, Department of Materials Science and Engineering, Indian Institute of Technology, Delhi, Hauz Khas, New Delhi 110016, India. Contact e-mails: rlnarayan@mse.iitd.ac.in and wzhanxjtu@mail.xjtu.edu.cn.

The microstructure of EBM or SLM fabricated Ti-6Al-4V consists of coplanar α and β, with both colony and basketweave morphology, within a columnar prior β grain (Ref 6, 7). The presence of α' martensite, which greatly enhances the strength and hardness, was also detected (Ref 6-9). However, regardless of the microstructure, process optimization and control over cooling rate in EBM and SLM processes ensures homogeneity in the Ti-6Al-4V microstructural features at all locations in the build, which in turn results in uniform mechanical properties. In contrast, although alloys printed by powder DED-based LMD processes have the same microstructural components, i.e., α+β or α' martensite needles within prior β grains, their sizes are non-uniform and vary along the build direction (Ref. 10). This is due to the higher gradient in the cooling rates of powder DED processes compared to that of powder bed processes. LMD fabricated Ti-6Al-4V is significantly stronger than EBM fabricated ones because of the former's finer microstructural features (Ref. 11). However, no studies have hitherto examined the influence of different microstructural components on the mechanical behavior of Ti-6Al-4V produced by powder bed and powder DED processes.

To address this aspect, we printed Ti-6Al-4V using LMD and EBM methods and conducted a study to understand the multi-scale microstructure-mechanical property correlations. Microstructural analysis was conducted using X-ray diffraction (XRD), scanning and transmission electron microscopy (SEM/TEM) while mechanical characterization was conducted via hardness and tensile tests. Samples fabricated by LMD are stronger and undergo significant strain hardening whereas EBM fabricated samples have lower strength but higher ductility. Moreover, the variation of hardness in EBM samples is homogeneous but that in LMD has a gradient along the build direction. These results are rationalized by articulating the role of various microstructural components in the deformation mechanisms of Ti-6Al-4V fabricated by these two AM methods.

## 2. Materials and Methods

Ti-6Al-4V samples were fabricated by laser metal deposition (LMD) and electron beam melting (EBM). Spherical gas atomized Grade 5 Ti-6Al-4V powders with particle sizes in the range of 45–106 $\mu$m were used for the fabrication of Ti-6Al-4V samples. In the LMD process, samples were built by depositing Ti-6Al-4V on a wrought Ti-6Al-4V substrate using Nd-YAG Laser (Ref. 12). The laser operates at a power of 30 W, has a beam diameter of 0.6 mm, and scanning velocity of 0.01 m/s. A constant powder flow rate of 2.5 g/min is maintained with a lap rate of 40%. Alternately, in the EBM technique, samples were built using the Arcam EBM system, wherein Ti-6Al-4V was deposited on a stainless steel substrate, which was held at 730 °C during the building process (Ref. 13). The Arcam EBM system uses a standard processing recipe for printing Ti-6Al-4V (Ref. 14). The operating voltage was 60 kV and beam current was 5 mA, beam diameter is approximately 1 mm and the scanning speed was 144 mm $s^{-1}$. The chamber pressure was maintained at 5 × $10^{-4}$ mbar. The LMD and EBM builds are cuboidal in shape and have the dimensions 18 mm × 10 mm × 3.5 mm and 50 mm × 13.5 mm × 3.5 mm (length × breadth × thickness), respectively. The densities of both samples were measured using Archimedes principle. XRD (**Bruker D8**), SEM (**SU6600**) and TEM (**JEM-2100F**) were used as characterization tools for microstructural analysis. Moreover, phases were analyzed by employing XRD, selected area electron diffraction (SAED) and element scans. SEM samples were ground, polished and etched in Kroll's reagent (2% HF, 6%$HNO_3$ and 92% $H_2O$) for 20 s. TEM samples were prepared by mechanical polishing and electron jet polishing with a solution of 5% $HClO_4$, 35% $CH_3OH$ and 60% $C_4H_9OH$. The top and bottom cross sections of the samples were studied using SEM and TEM. Hereafter, the two types of AM built samples will be referred to as LMD and EBM.

Micro-indentation and tensile tests were conducted for evaluating the mechanical properties of 3D printed Ti-6Al-4V. Hardness of LMD and EBM samples was measured using Vickers micro-indentation. Each measurement was performed by applying a peak load of 100 gf for 15 seconds. The LMD sample consists of 38 layers of deposited Ti-6Al-4V, where the thickness of each layer is 500 $\mu$m. In each layer, 36 indentations are made and the separation between any two adjacent indentations is 100 $\mu$m. Thus, in total 1368 indentations were made on LMD samples. Alternately, the EBM sample has 101 layers, each of which is 500 $\mu$m thick. Within each layer 28 indentations were made and the separation between two adjacent indents is 500 $\mu$m. Therefore, data from a total of 2828 indentations were collected from EBM samples. Uniaxial tension tests were conducted with 10 cylindrical dog-bone shaped samples whose dimensions were 7 mm × 4.16 mm × 0.58 mm. The tests were performed according to the ASTM E8 standard. The loading direction was parallel to the build direction. The side surfaces of all specimens were polished to a mirror finish. Tests were performed under displacement control with a rate 0.42 mm/min, which corresponds to a nominal quasi-static strain rate of 0.001 $s^{-1}$. The side surfaces and fracture surfaces were observed in the SEM.

## 3. Results

### 3.1 Microstructure of LMD and EBM Ti-6Al-4V

From density measurements, the volume fraction of pores for LMD and EBM samples were determined as 0.54 and 0.41 %, respectively. The XRD scans for LMD and EBM manufactured Ti-6Al-4V alloys are shown in Fig. 1. Diffraction peaks corresponding to multiple planes of α-Ti and a single (110) peak corresponding to $\beta$-Ti were indexed and labeled in both LMD and EBM samples. The presence of α and $\beta$ phase is expected in Ti-6Al-4V alloys as they are stabilized by Al and V, respectively. Compared to α and β peaks in EBM samples, those of the LMD samples are slightly shifted to lower $2\theta$. These peak shifts are an outcome of the higher cooling rate in LMD processes that leads to residual compressive stresses in the sample. Moreover, the XRD peaks obtained from both samples also exhibit broadening, which is attributed to small crystallite size and some internal strain. On measuring the extent of broadening and applying the Williamson–Hall method (Ref. 15), the average crystallite size of LMD and EBM specimens was calculated as 20.45 and 63.14 nm, respectively. The contribution of strain to peak broadening in LMD and EBM samples are only 0.01 and 0.00004%. Nevertheless, this can be used to calculate the individual dislocation densities in them (Ref. 15), which are 9.81× $10^8$ $m^{-2}$ and ∼4× $10^{14}$ $m^{-2}$, respectively. While there are no reports that have explicitly calculated the dislocation densities in EBM or LMD specimens, some of them mention that the residual stresses in EBM built specimens is negligible (Ref 16-19). This validates the comparatively lower dislocation density of the EBM specimen.

In addition to α and $\beta$ phase peaks, a (0016) peak corresponding to $\gamma$-Ti was also observed in the LMD sample but not in the EBM sample. To further examine these phases, SEM investigations of the two samples are conducted. Imaging was done at three portions of the builds in both samples, the top, middle and bottom. Figure 2(a-c) and Fig. 2(d–f) show the microstructures of the LMD and EBM samples, respectively. In the LMD sample, two orthogonal variants of a needle-like phase are observed at the bottom portion of the build, which extends from the substrate–sample interface to a length of 3 mm along the build direction. However, this morphology is absent in rest of the sample as the middle portion and top portion of the build contains only plate-type phases. In the middle portion, which is located between 4.5 mm from the top and 3 mm from the bottom of the build, most plates are arranged in a basketweave (Widmanstätten) pattern whereas the top portion of the build consists of colonies, with plates having

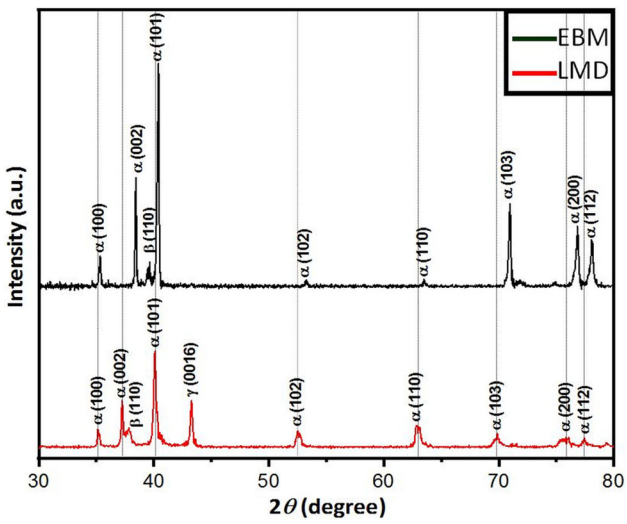


**Fig. 1** X-ray diffraction patterns of LMD and EBM built Ti6Al4V

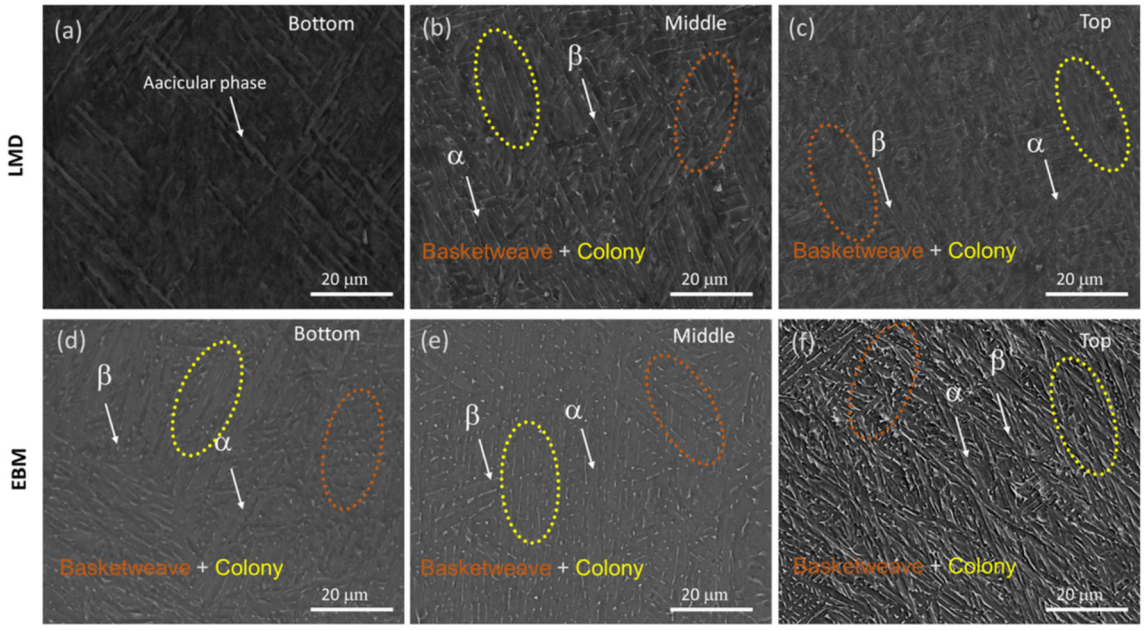


**Fig. 2** SEM images showing the microstructure of LMD prepared Ti-6Al-4V at (a) bottom and (b) middle and (c) top layer. (d-f) microstructures of EBM prepared Ti-6Al-4V at bottom, middle and top layer, respectively

a single orientation. Both microstructural morphologies have been highlighted with oval shaped colored bubbles on the microstructures. In contrast, the microstructure in the EBM sample has less distinct morphological variations and is a mix of basketweave and colony type plates at all locations in the build. Although regions with distinct microstructural transitions were not identified in EBM sample, boundaries of its bottom and top portions are marked at distances of 10 mm from the substrate and top of the build, respectively, purely for representative purposes. The basketweave and colony type morphologies are identified as variants of the α+β microstructure, where alternate α-Ti plates or laths are sandwiched between thinner $\beta$-laths.

To characterize the phases further, TEM imaging was performed on the bottom and top parts of the LMD and EBM samples. The TEM images of the bottom and top portions of the LMD sample is shown in Fig. 3(a and b), respectively. Their corresponding SAED patterns are shown as insets. At the bottom portion of the build, diffraction spots corresponding to the [01 $\bar{1}$ 0] and [01 $\bar{1}$] planes of α-Ti and $\beta$-Ti, respectively, were identified. The same phases were also identified at the top portion of the build. Moreover, the α-Ti in both portions of the build contain several dislocations, as marked by white arrows. Figure 3(c and d) shows the TEM images of the bottom and top portions of the EBM sample, respectively. Their corresponding SAED patterns reveal that both portions of the build in the EBM sample also contain α-Ti and $\beta$-Ti phases. However, a relatively lower dislocation density was observed in the EBM sample. Note that although a $\gamma$-Ti peak was detected in XRD scans, the corresponding phase could not be observed in SEM or TEM images. However, the formation of 2 nm sized $\gamma$-TiAl precipitates was also observed in Ti-6Al-4V processed by gas tungsten arc welding (GTAW), whose working principle is similar to metal AM (Ref. 20). Its formation was attributed to the segregation of Al in Ti during rapid cooling. A similar effect may have resulted in the formation of $\gamma$-TiAl in LMD samples and given that they are considerably fine, we were unable to resolve them.

Further TEM analysis followed by energy dispersive spectrometry (EDS) is conducted to determine the dimensions and composition of individual phases in the two samples. Figure 4(a–d) displays the bright field TEM images of the bottom and top portions of the LMD and EBM samples, respectively. From these images, the widths of α-Ti and $\beta$-Ti are measured and listed in Table 1. In the bottom portion of the LMD sample, the widths of α-Ti and $\beta$-Ti are 320 ±55 nm and 111 ± 33 nm. While the width of $\beta$-Ti remains the same in the top portion, α-Ti is more than twice as wide as that in the bottom portion (see Fig. 4b). In contrast, in both portions of the EBM sample, the width of α-Ti and $\beta$-Ti is ~620 and ~112 nm, respectively. The average lath widths of the two phases are also consistent with that observed in XRD.

Composition measurements were taken from locations within α-Ti and $\beta$-Ti marked in Fig. 4 and listed in Table 1. In LMD samples, α-Ti in both portions of the build contain ~6–7 at% of Al and ~4–6 at% V. In contrast, $\beta$-Ti in the bottom portion of the build has ~22.7 at% of V, which is about 3.5 times higher than that in the top portion of the build. The concentration of Al in $\beta$-Ti, measured in the top portion of the build, is slightly higher than expected because a part of α-Ti is included in the measurement field of EDS (see Fig. 4b). β-Ti in the bottom and top portion of the EBM samples contains ~7.29 at% and ~3.5 at% of V, respectively. Although the former has a relatively high content of V, it is significantly lesser than that in the bottom portion of the LMD sample. However, apart from this minor difference, concentrations of Al and V in α-Ti and $\beta$-Ti are relatively uniform in both portions of the EBM sample.

Overall, both samples have similar volume fraction of pores and prior $\beta$ grain widths. However, the morphology, widths and composition of the phases in the α+β microstructure of LMD samples vary along the build direction, whereas those of the EBM samples are relatively uniform. All α-Ti, except those at the bottom of the LMD samples, have similar widths. Also, the residual strain from the relatively higher cooling rates in LMD samples manifests as a higher dislocation density in α-Ti than that in EBM samples.

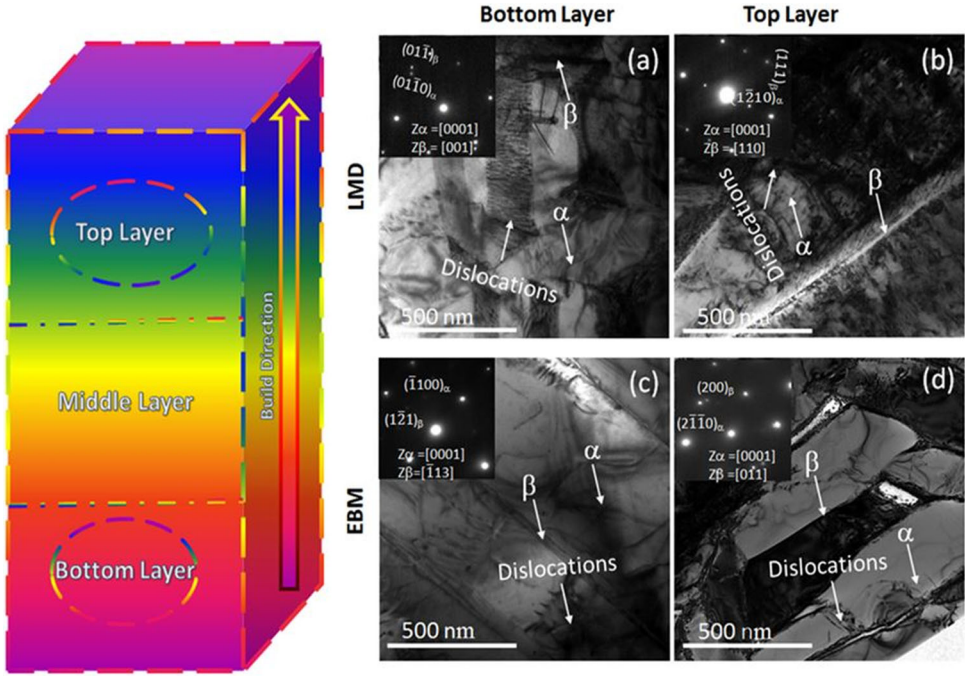


**Fig. 3** TEM images from (a) top layer and (b) bottom layer of LMD specimen and (c) top layer and (d) bottom layer of EBM specimen. The insets are SAED pattern taken from a and ß laths. (Left) Illustration of the build direction and bottom, middle and top layers

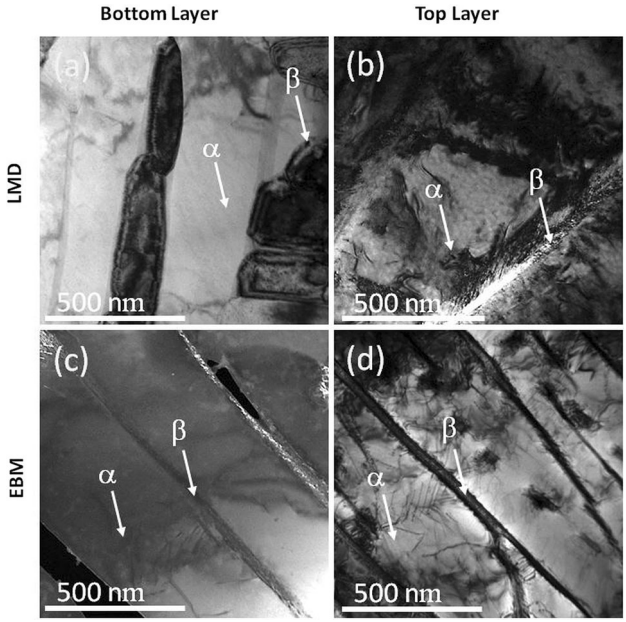


**Fig. 4** Bright field TEM images of (a-b) LMD prepared Ti-6Al-4V and (c-d) EBM built Ti-6Al-4V. Arrows show approximate locations where EDS was performed.

### 3.2 Mechanical Properties of LMD and EMB Ti-6Al-4V

**3.2.1 Hardness and Tensile Tests.** The spatial distribution of hardness, $H$, in LMD and EBM samples is shown Fig. 5. Regions corresponding to the top, middle and bottom portions of the build have been marked for reference. The bottom portion of the LMD sample is the hardest and has $H$=4.43 ±0.21 GPa, whereas $H$=3.87 ±0.32 GPa and 3.43 ±0.27 GPa in the middle and top portions, respectively. In contrast, $H$ in different portions of the EBM sample are similar; $H$ = 3.50 ±0.22 GPa in the bottom and 3.40 ±0.16 GPa and 3.24 ±0.33 GPa in the middle and top portions. Also, while the difference in $H$ at the top and bottom layer in LMD sample is ∼1 GPa, that in EBM samples is within the scatter in measurements. Previous studies indicate that $H$ of Ti-6Al-4V is in the range of 3.1–4.3GPa (Ref 21, 22). However, some studies reported a higher average $H$ due to the formation of α` (Ref. 21).

Representative engineering stress, $\sigma$, vs. engineering strain, $\varepsilon$, responses of the LMD and EBM samples are shown in Fig. 6(a). Their elastic responses are similar and the Young's modulus, $E$=125 GPa, reasonably matches with that of conventionally manufactured Ti-6Al-4V (Ref 23). However, the plastic deformation characteristics of the two alloys are distinctly different. The LMD and EBM samples have yield strengths of ∼1020 ± 13 MPa and ∼890 ± 15 MPa, respectively. LMD sample also undergoes significant strain hardening and attains an ultimate tensile strength (UTS) of 1100 ±9 MPa, whereas the EBM sample attains an UTS of only 930 ±22 MPa. Alternately, the EBM sample has a higher strain to failure, $\varepsilon_f$ ∼0.11, whereas the LMD sample breaks at $\varepsilon_f$ ∼0.08. It was reported that the mechanical properties of Ti-6Al-4V (with $\alpha$+$\beta$ microstructure) produced by EBM is comparable to that produced by conventional methods (Ref 24). LMD samples, on the other hand, are significantly stronger than those manufactured by conventional manufacturing methods as well as by AM methods, such as SLM.

The work hardening behavior of the two alloys is further investigated by fitting the portion of the flow curves between YS and UTS with the following power law: $\sigma^T = K(\varepsilon^T)^n$, where $K$ is a constant, $\sigma^T$ is the true stress, and $\varepsilon^T$ is the true strain and $n$ is the strain hardening exponent. According to Considère's criterion for necking (Ref. 25), the total uniform strain, $\varepsilon_u$, a material can experience is equal to $n$. In Table 2, for both samples, the values of $n$, the coefficient of determination for the fit, $R^2$, and $\varepsilon_u$, which

**Table 1 Compositions and width of α and β in different portions of the LMD and EBM samples**

| Constituent | LMD sample | | | | EBM sample | | | |
|---|---|---|---|---|---|---|---|---|
| | Bottom portion | | Top portion | | Bottom portion | | Top portion | |
| | α | *B* | α | β | α | β | α | β |
| Al (at%), CuK | 6.96 | 2.48 | 6.36 | 5.44 | 5.21 | 4.25 | 5.65 | 4.87 |
| V (at%), CuK | 3.24 | 22.65 | 6.09 | 6.01 | 2.86 | 7.29 | 3.22 | 3.50 |
| Width, nm | 320 ± 60 | 111 ± 33 | 650 ± 21 | 115 ± 23 | 615 ± 50 | 109 ± 17 | 630 ± 32 | 112 ± 20 |

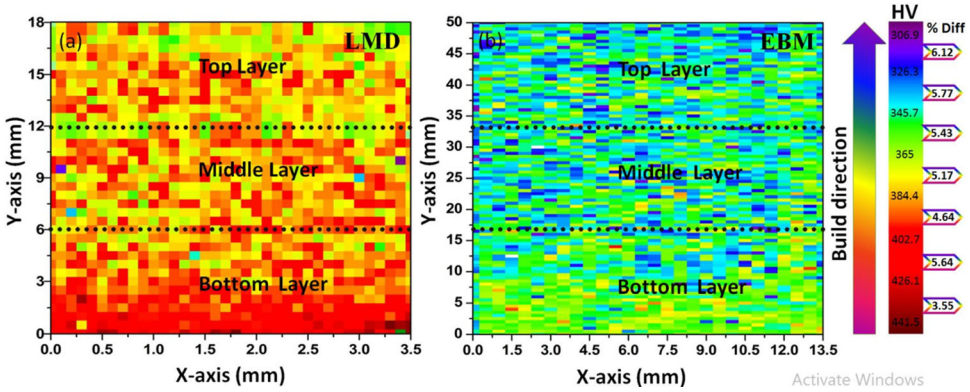


**Fig. 5** Micro-indentation mapping of (a) LMD Ti-6Al-4V and (b) EBM Ti-6Al-4V showing hardness variations in the builds

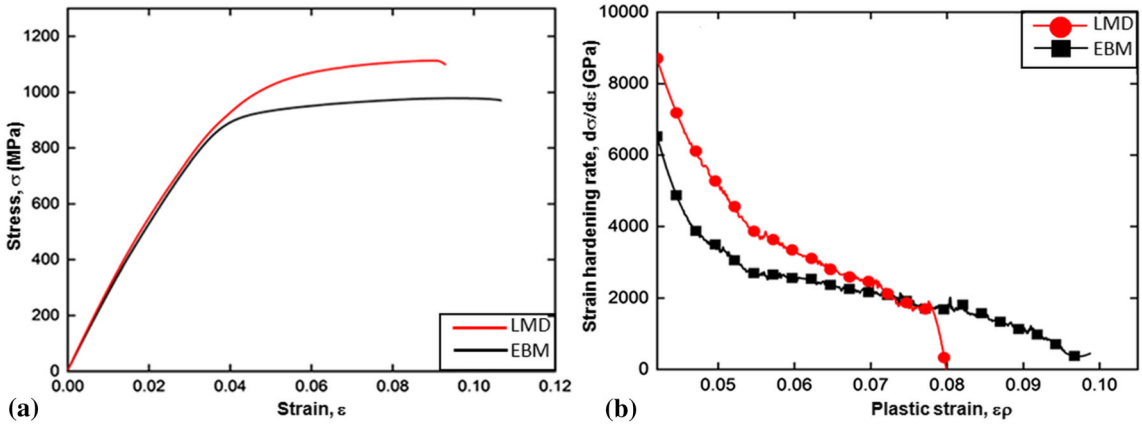


**Fig. 6** (a) Tensile stress–strain curves of LMD and EBM manufactured Ti-6Al-4V and (b) their strain hardening rate, ds/de, as a function of true plastic strain, $e_p$

is the same as their respective $\varepsilon_f$*, are listed. The equation fits the flow curves of both samples well as $R^2$ ~0.99. Moreover, for the EBM sample, $n$ ~0.14 and $\varepsilon_u$ ~0.11, which match reasonably well. In contrast, although the LMD sample has a larger $n$ ~0.18, the value of $\varepsilon_u$ is 56% lesser than expected.

To further understand the hardening behavior of both samples, the variations in strain hardening rate, $d\sigma/d\varepsilon$, are determined. As shown in Fig. 6(b), $d\sigma/d\varepsilon$ is plotted as a function of plastic strain, $\varepsilon_p$ ($=\varepsilon_u-\varepsilon_y$). Note that at $\varepsilon_p$ = 0,LMD sample exhibits higher $d\sigma/d\varepsilon$ than that of EBM sample. However, the rate at which $d\sigma/d\varepsilon$ decreases with increasing $\varepsilon_p$ is higher in the LMD sample. An outcome of this is that

*Since both samples exhibit negligible post-necking plasticity, their corresponding $\varepsilon_f$ and $\varepsilon_u$ are the same.

**Table 2 The obtained total strain before necking, $\varepsilon_u$, the calculated strain exponents, *n*, and coefficient determination, $R^2$, of LMD and EBM samples**

| Sample type | $\varepsilon_u$ | *n* | $R^2$ |
|---|---|---|---|
| LMD | 0.08 | 0.186 | 0.99 |
| EBM | 0.11 | 0.144 | 0.99 |

$d\sigma/d\varepsilon$ of both samples become equal at $\varepsilon_p$= 0.075. Thereafter, with increasing $\varepsilon_p$, $d\sigma/d\varepsilon$ of the LMD sample drops rapidly whereas that of EBM sample decreases gradually. Overall, Ti-6Al-4V printed by LMD is harder, stronger and has better hardenability than that printed by EBM. Alternately, EBM-

printed Ti-6Al-4V part has more uniform hardness throughout the build and exhibits better ductility.

**3.2.2 Fractography and Post Facto Microstructure Characterization.** To assess the nature of failure, post facto imaging of the tensile-tested samples is performed. Figure 7(a) displays the SEM images of side surfaces of the LMD tensile samples after failure. Shear bands were observed on the LMD sample surface but the same were not observed on EBM samples. The fracture surfaces of the LMD and EBM tensile samples are shown in Fig. 7(b and c). Macroscopic pores are observed in both samples. The fracture surfaces of both samples consist mainly of ductile fracture features such as dimples. The TEM images of the tensile-tested LMD and EBM samples are shown in Fig. 8. Distinct slip lines within α-laths indicate that planar slip on basal, pyramidal and prismatic planes occurs. The sharp lines in Fig. 8 were confirmed to be slip lines when they disappeared after the specimen was tilted to 5°, as shown in Fig. 9. This is because the dislocations no longer satisfy the diffraction condition. However, the α-laths in LMD sample have a greater number of slip steps and dislocation density than that in the EBM sample.

## 4. Discussion

### 4.1 Microstructural Evolution of LMD and EBM Ti-6Al-4V

According to the phase diagram of Ti-6Al-4V, cooling from the melt first leads to the formation of columnar $\beta$ grains (Ref. 26). When the temperature drops below the $\beta$ transus, this β grain transforms to either of $\alpha$'-Ti or $\alpha+\beta$ phase, depending on the cooling rate (Ref 27, 28). At high cooling rates, the martensitic $\alpha$'-Ti phase with an acicular or needle-like morphology forms. $\alpha$'-Ti is a nonequilibrium phase that was first reported by Yang et al. (Ref. 29). Its formation is favored during rapid solidification of Ti-6Al-4V from the melt or in the presence of steep thermal gradients. At intermediately lower cooling rates, diffusion occurs and a coplanar $\alpha+\beta$ lamellar microstructure forms inside the prior $\beta$ grains. Even subtle variations in this cooling rate regime lead to the formation of different $\alpha + \beta$ morphologies. At relatively higher cooling rates, the $\alpha + \beta$ microstructure has a 'basketweave' or Widmanstätten morphology where multiple colonies of $\alpha + \beta$, with different orientations, mutually intersect. As the cooling rate reduces, only one specific colony of the $\alpha + \beta$ phase grows, either from the prior β grain boundary or from the allotriomorphic α phase at the boundary (Ref. 30).

The above-mentioned mechanism provides a basis for the observed microstructural features observed in the LMD and EBM samples. Comparing the power input and scan velocities of EBM and LMD, it is evident that the cooling rate is significantly lower in the former than that in latter. However, when the temperature drops below the $\beta$ transus, the size and orientation of the columnar $\beta$ grains are unaffected by the difference in cooling rates. Therefore, the prior β grains have an average width of $\sim$250 $\mu$m and $<001>$ texture in both samples (Ref 2). Since the bottom portion of the LMD sample experiences the fastest cooling rate, it is likely to facilitate the

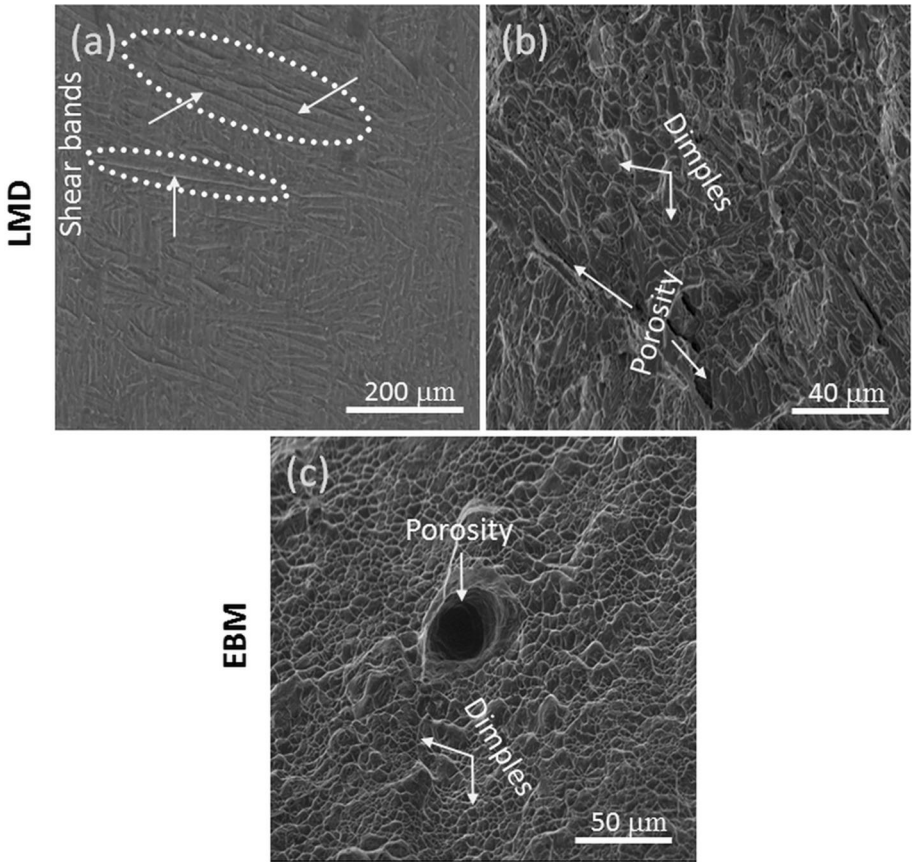


**Fig. 7** SEM micrographs of side surfaces of tensile tested (a) LMD specimen and fracture surfaces of (b) LMD and (c) EBM specimens of Ti6Al4V

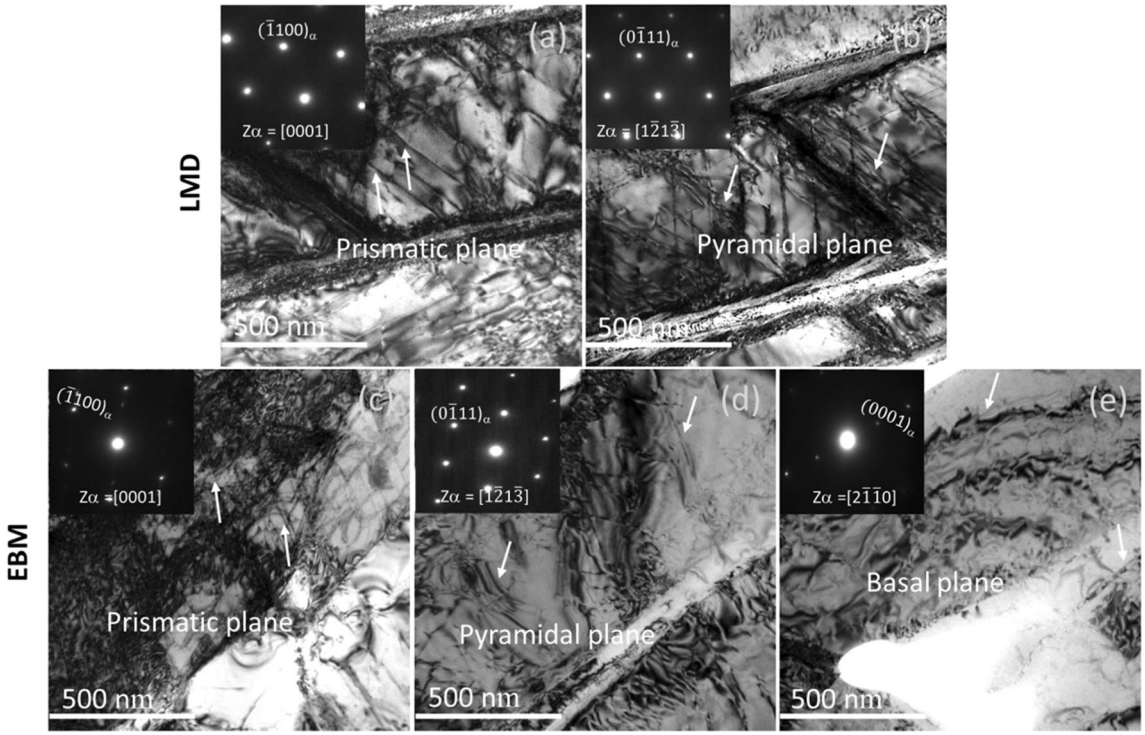


**Fig. 8** TEM images of deformed (a-b) LMD Ti-6Al-4V specimen and (c-e) EBM Ti-6Al-4V specimens

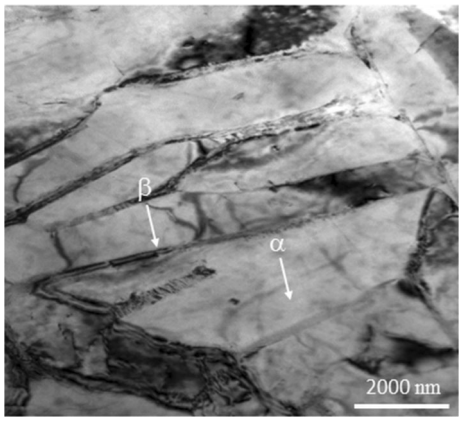


**Fig. 9** Bright field TEM image of deformed LMD Ti-6Al-4V specimen after tilting to 5°

formation of α'-Ti. Although needle-like precipitates, resembling α'-Ti, were observed in SEM images at this location (see Fig. 2a), XRD scans could not confirm its presence. It is possible that XRD may not be reliable in detecting this phase as its crystal structure and lattice parameters closely resemble α-Ti (Ref. 31). However, subsequent TEM imaging confirmed that the bottom portion of the specimen only contains α-Ti and β-Ti (see Fig. 3a). Interestingly, EDS revealed that β-Ti at this location was supersaturated in V, which is actually a characteristic feature of the α'-Ti phase. The likely explanation for these observations is that the α'-Ti martensite phase would have formed initially at the bottom part of the build due to rapid cooling. However, with increasing build height and continued scanning, heat would have accumulated in the sample, as Ti-6Al-4V has relatively low thermal conductivity (Ref. 32). This prolonged exposure to heat could have partially decomposed the α'-Ti to α-Ti and β-Ti, without significantly altering its initial morphology (Ref. 33). In fact, prior studies confirm that decomposition of α'-Ti to α-Ti and β-Ti (Ref 31, 34, 35) can indeed occur in the temperature range of 600–650 °C (Ref 36-38).

Accumulation of heat in the build with increasing height also implies that the middle and top parts will experience a progressively lower cooling rate. Therefore, the middle and top parts of the build are expected to have an α + β microstructure with basketweave and colony morphologies, respectively. In contrast, when EBM samples are fabricated, the substrate temperature is constantly maintained at 730 °C. As a result, the cooling rate in the entire build, including the bottom layer, is relatively lower, which in turn ensures the formation of a colony type α+β microstructure interspersed with basketweave type α + β.

### 4.2 Deformation Mechanisms in LMD and EBM Ti-6Al-4V

The prior β grains and α + β microstructure are primary microstructural features determine the deformation mechanisms of Ti-6Al-4V. Fine equiaxed prior β grains exhibit higher strength and ductility compared to large columnar ones (Ref 33, 39). Since both samples in this study contain columnar prior β grains of similar sizes, mechanical property differences between them are more likely to be associated with the characteristics of α and β laths, and the residual strain in them, which is characterized by the dislocation density. α-Ti exhibits wide variations in both samples whereas β-Ti has a fixed size. The bottom portion of the LMD sample has the finest α-Ti sizes, which reduces the effective dislocation slip length, and is therefore expectedly the hardest. The hardness is also enhanced

by excess V content in $\beta$-Ti, which leads to its solid solution strengthening.

The significant decrease in $H$ along the build direction is an outcome of the steady increase in the width of α-Ti at the upper portions of the LMD sample. In contrast, the EBM sample has relatively uniform $H$ at all locations of the build owing to the constant α-Ti widths. However, the middle and top portions of the LMD sample, despite having the similar α-Ti widths as that of EBM sample, are slightly harder. This difference in $H$ is attributed to the higher dislocation content and residual strains within α-Ti of LMD samples (see Fig. 4b) due to the higher cooling rates (see section 3.1).

Similarly, the higher tensile strength of LMD samples compared to that of EMB samples is the outcome of the higher dislocation content in the former's α-Ti, which acts as barriers for dislocation slip. The higher resistance to dislocation motion in the former is also the reason why its $n$ is higher. The relative differences in the $\alpha + \beta$ morphologies, i.e., Widmanstätten or colony type, also affects the hardening behavior of Ti-6Al-4V as follows. In the basketweave or Widmanstätten morphology, α laths are intersected by laths of other orientations, which limits their average lengths compared to those in a colony type microstructure. Consequently, hardening due to dislocation slip in the basketweave α laths saturates at significantly lower strains than that in the colony type α laths (Ref 33, 39). This implies that $d\sigma/d\varepsilon$ in basketweave morphology dominated $\alpha + \beta$ microstructure will reduce rapidly. In contrast, owing to the longer lengths of α laths, the drop in $d\sigma/d\varepsilon$ in a colony type $\alpha + \beta$ microstructure will be more gradual.

This explains why the $d\sigma/d\varepsilon$ of EBM sample, which has a larger proportion of the colony type $\alpha + \beta$ morphology in its microstructure, reduces gradually compared to that of the LMD sample. In fact, the observation of a relatively higher density of dislocations and slip steps in α-Ti of deformed LMD samples implies that hardening saturation has occurred, which lends further support to this argument. Nevertheless, owing to a higher value of $n$, the $\varepsilon_u$ of LMD sample is still expected to higher than that of the EBM sample. Hardening saturation in the basketweave α laths of the LMD sample is followed by rapid strain localization. The observation of shear bands in Fig. 7(b) provides further evidence for strain localization in the LMD sample. This strain localization increases the susceptibility of premature failure in the LMD sample. Therefore, even though the volume fraction of pores in both samples is similar, LMD samples fail prematurely. It is also worth mentioning that despite having an hcp crystal structure, the deformation in α is governed by dislocation slip and not twinning. It is possible that the absence of deformation twins is an outcome of the distortion introduced in α lathes, which in turn enhances the critically resolved shear stress for twinning.

Based on these observations, the following strategies can be employed to improve the performance of EBM and LMD manufactured Ti-6Al-4V. The gradient in the hardness of an alloy manufactured by LMD has to be relieved by performing heat treatments. However, an appropriate heat treatment, which does not compromise the average hardness must be chosen. Moreover, while the strength and hardness of alloys manufactured by LMD are optimum, their ductility could be potentially improved by identifying a process space that minimizes the volume fraction of pores and increases the proportion of colony type $\alpha + \beta$ microstructure. An alternate solution is to conduct hot isostatic pressing of LMD manufactured components after printing. In contrast, although alloys printed by EBM are microstructurally homogeneous and as a result have uniform mechanical properties, their strengths have further scope for improvement. Increasing the cooling rate to obtain α laths with higher dislocation density is not an option as higher cooling rates also promote the formation of the basketweave microstructure. The only viable alternative that was proposed by Kumar et al. for SLM printed Ti-6Al-4V is to minimize the prior-β grain size by choosing an optimal scanning strategy (Ref 39, 40). Finally, in the context of choosing an AM process for repairing damaged components, we would like to emphasize that it is not prudent to rely only on this study as both processes allow an additional process parameter modifications. However, if the standard machine-manufacturer specific recipe is considered, while LMD is more suitable than EBM from the process design perspective, its success hinges on choosing the appropriate post-processing treatments that optimizes their performance.

## 5. Conclusions

Ti-6Al-4V printed by LMD and EBM produce an α+β microstructure within prior $\beta$ columnar grains and have similar porosities. However, the differences in the cooling profiles of both processes influences the composition, morphology and length scales of the $\alpha + \beta$ microstructure. A non-uniform and fast cooling rate, such as that in LMD samples, introduces a gradient in the microstructure and hardness but also increases the dislocation density in α, which in turn improves the strength and hardenability. A basketweave microstructure undergoes faster hardening saturation and localization compared to that of a colony type morphology. This localization can even offset a higher value of strain hardening exponent and lead to premature failure. Process modifications to obtain the best combination of mechanical properties should aim to produce a microstructure that has a combination of finer α-Ti with high dislocation density and a columnar α+β morphology.


### Acknowledgments

We appreciate Dr. Gang Chen and Prof. Anfeng Zhang for providing the LMD and EMB Ti-6Al-4V samples, respectively. This work was supported by the CSC Master program.


### Declaration

### Conflict of interest

The authors declare no conflict of interest.

### References


1. D.T. Pham and R.S. Gault, A Comparison of Rapid Prototyping Technologies, *Int. J. Mach. Tools Manuf.*, 1998, **38**(10–11), 1257–1287
2. X. Tan, Y. Kok, Y.J. Tan, M. Descoins, D. Mangelinck, S.B. Tor, K.F. Leong and C.K. Chua, Graded Microstructure and Mechanical Properties of Additive Manufactured Ti-6Al-4V via Electron Beam Melting, *Acta Mater.*, 2015, **97**, 1–16. https://doi.org/10.1016/j.actamat.2015.06.036
3. L.E. Murr, E.V. Esquivel, S.A. Quinones, S.M. Gaytan, M.I. Lopez, E.Y. Martinez, F. Medina, D.H. Hernandez, E. Martinez, J.L. Martinez,

S.W. Stafford, D.K. Brown, T. Hoppe, W. Meyers, U. Lindhe and R.B. Wicker, Microstructures and Mechanical Properties of Electron Beam-Rapid Manufactured Ti-6Al-4V Biomedical Prototypes Compared to Wrought Ti-6Al-4V, *Mater. Charact*, 2009, **60**(2), 96–105. https://doi.org/10.1016/j.matchar.2008.07.006

4. A. Paolini, S. Kollmannsberger and E. Rank, Additive Manufacturing in Construction: A Review on Processes, Applications, and Digital Planning Methods, *Addit. Manuf.*, 2019, **30**, 100894. https://doi.org/10.1016/j.addma.2019.100894
5. M. Seifi, A. Salem, J. Beuth, O. Harrysson and J.J. Lewandowski, Overview of Materials Qualification Needs for Metal Additive Manufacturing, *Jom*, 2016, **68**(3), 747–764
6. S.S. Al-Bermani, M.L. Blackmore, W. Zhang and I. Todd, The Origin of Microstructural Diversity, Texture, and Mechanical Properties in Electron Beam Melted Ti-6Al-4V, *Metall. Mater. Trans. A Phys. Metall. Mater. Sci.*, 2010, **41**(13), 3422–3434
7. Y. Kok, X. Tan, S.B. Tor and C.K. Chua, Fabrication and Microstructural Characterisation of Additive Manufactured Ti-6Al-4V Parts by Electron Beam Melting, *Virtual Phys. Prototyp.*, 2015, **10**(1), 13–21
8. N. Hrabe and T. Quinn, Effects of Processing on Microstructure and Mechanical Properties of a Titanium Alloy (Ti-6Al-4V) Fabricated Using Electron Beam Melting (EBM), Part 1: Distance from Build Plate and Part Size, *Mater. Sci. Eng. A*, 2013, **573**, 264–270. https://doi.org/10.1016/j.msea.2013.02.064
9. L.E. Murr, S.M. Gaytan, F. Medina, E. Martinez, J.L. Martinez, D.H. Hernandez, B.I. Machado, D.A. Ramirez and R.B. Wicker, Characterization of Ti-6Al-4V Open Cellular Foams Fabricated by Additive Manufacturing Using Electron Beam Melting, *Mater. Sci. Eng. A*, 2010, **527**(7–8), 1861–1868. https://doi.org/10.1016/j.msea.2009.11.015
10. S. Liu and Y.C. Shin, Additive Manufacturing of Ti6Al4V Alloy: A Review, *Mater. Des.*, 2019, **164**, 107552. https://doi.org/10.1016/j.matdes.2018.107552
11. M. Thomas, T. Malot, P. Aubry, C. Colin, T. Vilaro and P. Bertrand, The Prospects for Additive Manufacturing of Bulk TiAl Alloy, *Mater. High Temp.*, 2016, **33**(4–5), 571–577
12. L.D. Shi Bofei, Z. Anfeng and Q. Baolu, Influence of Heat Accumulation on Microstructure and Property of Ti-6Al-4V in Laser Direct Forming, *Laser Technol.*, 2016, **40**(1), 29–32. https://doi.org/10.7510/jgjs.issn.1001-3806.2016.01.007
13. J. Wang, H.P. Tang, K. Yang, N. Liu, L. Jia and M. Qian, Selective Electron Beam Manufacturing of Ti-6Al-4V Strips: Effect of Build Orientation Columnar Grain Orientation, and Hot Isostatic Pressing on Tensile Properties, *J Miner MEt Mater Soc.*, 2018, **70**(5), 638–643. https://doi.org/10.1007/s11837-018-2794-3
14. C. Pirozzi, S. Franchitti, R. Borrelli, G. Diodati and G. Vattasso, Experimental Study on the Porosity of Electron Beam Melting-Manufactured Ti6Al4V, *J. Mater. Eng. Perform.*, 2019, **28**(5), 2649–2660. https://doi.org/10.1007/s11665-019-04038-7
15. P. Bindu and S. Thomas, Estimation of Lattice Strain in ZnO Nanoparticles: X-Ray Peak Profile Analysis, *J. Theor. Appl. Phys.*, 2014, **8**, 123–134. https://doi.org/10.1007/s40094-014-0141-9
16. W. He, W. Jia, H. Liu, H. Tang, X. Kang and Y. Huang, Research on Preheating of Titanium Alloy Powder in Electron Beam Melting Technology, *Xiyou Jinshu Cailiao Yu Gongcheng/Rare Met, Mater. Eng.*, 2011, **40**(12), 2072–2075
17. V. Chastand, P. Quaegebeur, W. Maia and E. Charkaluk, Comparative Study of Fatigue Properties of Ti-6Al-4V Specimens Built by Electron Beam Melting (EBM) and Selective Laser Melting (SLM), *Mater. Charact.*, 2018, **143**, 76–81
18. Y. Zhai, H. Galarraga and D.A. Lados, Microstructure, Static Properties, and Fatigue Crack Growth Mechanisms in Ti-6Al-4V Fabricated by Additive Manufacturing: LENS and EBM, *Eng. Fail. Anal.*, 2016, **69**, 3–14
19. N. Hrabe, T. Gnäupel-Herold and T. Quinn, Fatigue Properties of a Titanium Alloy (Ti–6Al–4V) Fabricated via Electron Beam Melting (EBM): Effects of Internal Defects and Residual Stress, *Int. J. Fatigue*, 2017, **94**, 202–210
20. L.M. Wang, H.C. Lin and C.J. Tsai, Characterization and Mechanism of A2-Ti3Al and γ-TiAl Precipitation in Ti-6Al-4V Alloy Following Tungsten Arc Welding, *Key Eng. Mater.*, 2012, **520**, 320–329
21. L.E. Murr, S.M. Gaytan, M.I. Lopez, E. Martinez, F. Medina and R.B. Wicker, Metallographic Characterization of Additive-Layer Manufactured Products by Electron Beam Melting of Ti-6Al-4V Powder, *Practical Metallography*, 2009, **46**(9), 442–453. https://doi.org/10.3139/147.110036
22. L. Facchini, E. Magalini, P. Robotti and A. Molinari, Microstructure and Mechanical Properties of Ti-6Al-4V Produced by Electron Beam Melting of Pre-Alloyed Powders, *Rapid Prototyp. J.*, 2009, **15**(3), 171–178
23. B. Baufeld and O. Van Der Biest, Mechanical Properties of Ti-6Al-4V Specimens Produced by Shaped Metal Deposition, *Sci. Technol. Adv. Mater.*, 2009, **10**(1), 015008. https://doi.org/10.1088/1468-6996/10/1/015008
24. Y.M. Ren, X. Lin, X. Fu, H. Tan, J. Chen and W.D. Huang, Microstructure and Deformation Behavior of Ti-6Al-4V Alloy by High-Power Laser Solid Forming, *Acta Mater.*, 2017, **132**, 82–95
25. G.E. Dieter and D. Bacon, Mechanical Metallurgy SI Metric Edition, *J. Franklin Inst.*, 1988, 766
26. A. Ducato, L. Fratini, M. La Cascia and G. Mazzola, An Automated Visual Inspection System for the Classification of the Phases of Ti-6Al-4V Titanium Alloy, *Lect. Notes Comput. Sci. (including Subser Lect. Notes Artif. Intell. Lect. Notes Bioinformatics)*, 2013, **8048**, 362–369
27. G. Lütjering, Influence of Processing on Microstructure and Mechanical Properties of ($\alpha + \beta$) Titanium Alloys, *Mater. Sci. Eng. A*, 1998, **243**(1–2), 32–45
28. T. Ahmed and H.J. Rack, Phase Transformations during Cooling in $\alpha + \beta$ Titanium Alloys, *Mater. Sci. Eng. A*, 1998, **243**(1–2), 206–211
29. J. Yang, H. Yu, J. Yin, M. Gao, Z. Wang and X. Zeng, Formation and Control of Martensite in Ti-6Al-4V Alloy Produced by Selective Laser Melting, *Mater. Des.*, 2016, **108**, 308–318. https://doi.org/10.1016/j.matdes.2016.06.117
30. B. Appolaire, L. Héricher and E. Aeby-Gautier, Modelling of Phase Transformation Kinetics in Ti Alloys-Isothermal Treatments, *Acta Mater.*, 2005, **53**(10), 3001–3011
31. Y. Mantani and M. Tajima, Phase Transformation of Quenched A″ Martensite by Aging in Ti-Nb Alloys, *Mater. Sci. Eng. A*, 2006, **438–440**, 315–319. https://doi.org/10.1016/j.msea.2006.02.180
32. L. Parry, I.A. Ashcroft and R.D. Wildman, Understanding the Effect of Laser Scan Strategy on Residual Stress in Selective Laser Melting through Thermo-Mechanical Simulation, *Addit. Manuf.*, 2016, **12**, 1–15
33. A. Safdar, L.Y. Wei, A. Snis and Z. Lai, Evaluation of Microstructural Development in Electron Beam Melted Ti-6Al-4V, *Mater. Charact.*, 2012, **65**, 8–15. https://doi.org/10.1016/j.matchar.2011.12.008
34. K. Sato, H. Matsumoto, K. Kodaira, T.J. Konno and A. Chiba, Phase Transformation and Age-Hardening of Hexagonal A′ Martensite in Ti-12 Mass%V-2 Mass%Al Alloys Studied by Transmission Electron Microscopy, *J. Alloys Compd.*, 2010, **506**(2), 607–614. https://doi.org/10.1016/j.jallcom.2010.07.127
35. X. Tan, Y. Kok, Y.J. Tan, G. Vastola, Q.X. Pei, G. Zhang, Y.W. Zhang, S.B. Tor, K.F. Leong and C.K. Chua, An Experimental and Simulation Study on Build Thickness Dependent Microstructure for Electron Beam Melted Ti-6Al-4V, *J. Alloys Compd.*, 2015, **646**, 303–309. https://doi.org/10.1016/j.jallcom.2015.05.178
36. P. Vora, K. Mumtaz, I. Todd and N. Hopkinson, AlSi12 In-Situ Alloy Formation and Residual Stress Reduction Using Anchorless Selective Laser Melting, *Addit. Manuf.*, 2015, **7**, 12–19. https://doi.org/10.1016/j.addma.2015.06.003
37. W. Xu, M. Brandt, S. Sun, J. Elambasseril, Q. Liu, K. Latham, K. Xia and M. Qian, Additive Manufacturing of Strong and Ductile Ti-6Al-4V by Selective Laser Melting via in Situ Martensite Decomposition, *Acta Mater.*, 2015, **85**, 74–84. https://doi.org/10.1016/j.actamat.2014.11.028
38. H. Gong, K. Rafi, H. Gu, G.D. Janaki Ram, T. Starr and B. Stucker, Influence of Defects on Mechanical Properties of Ti-6Al-4V Components Produced by Selective Laser Melting and Electron Beam Melting, *Mater. Des.*, 2015, **86**, 545–554. https://doi.org/10.1016/j.matdes.2015.07.147

39. P. Kumar, O. Prakash and U. Ramamurty, Micro-and Meso-Structures and Their Influence on Mechanical Properties of Selectively Laser Melted Ti-6Al-4V, *Acta Mater.*, 2018, **154**, 246–260. https://doi.org/10.1016/j.actamat.2018.05.044
40. P. Kumar and U. Ramamurty, Microstructural Optimization through Heat Treatment for Enhancing the Fracture Toughness and Fatigue Crack Growth Resistance of Selective Laser Melted Ti–6Al–4V Alloy, *Acta Mater.*, 2019, **169**, 45–59. https://doi.org/10.1016/j.actamat.2019.03.003